Thermoelectric performance optimization of GeMnSbTe compounds through increasing the Mn solid solubility: Effects of the co-doping of rare earth elements

Wenjing Huang [a], Feida Chen [a,b,*], Shujie Wu [a], Xiaobin Tang [a,b,*]

[a] Department of Nuclear Science and Technology, Nanjing University of Aeronautics and Astronautics, 211100, China
[b] Key Laboratory of Nuclear Technology Application and Radiation Protection in Astronautics, Ministry of Industry and Information Technology, Nanjing 211106, China

ABSTRACT

GeTe is a p-type thermoelectric (TE) material that exhibits a high ZT value and holds promise for a wide range of applications. In this study, a series of $Ge_{0.86}Mn_{0.1}Sb_{0.04}Te$ + 1 mol.% RE (Rare Earth elements = Er, Tm, Yb, Lu) compounds are synthesized through the melt-quenching method followed by fast-hot-pressing. Findings indicate that the TE properties are improved by simultaneously increasing the Seebeck coefficient and reducing the thermal conductivity, making the peak ZT value experiences an enhancement of 73%, while the average ZT value through 450–800 K shows an improvement of 70%. The solid solubility of Mn is significantly increased by the addition of the REs, that promotes the regulating effect of Mn on the energy band. A diverse range of microstructures including ordered atomic staggered arrays, van der Waals interstitials, dislocation enrichment, dislocation networks, nano precipitation phases with cavity structures, interstitial clusters, and vacancy clusters are introduced by REs, significantly contributing to the reduction of the κ_L. Thus, this study offers valuable insights and mechanism analysis into enhancing the properties of GeMnSbTe materials by incorporating REs, and proves that Tm has better thermoelectric performance optimization effect in this.

1. Introduction

Waste heat is inevitably generated in energy conversion processes [1]. The discovery of the thermoelectric (TE) effect and the development of TE materials have enabled the recovery of the waste heat from industrial waste heat, automobile exhaust, or even hot mobile phones and the human body, offering a clean and sustainable energy technology for future energy revolution [2–5]. Additionally, due to their advantages, such as pollution-free operation, absence of mechanical vibration, and high reliability, TE technology has gained considerable attention in the field of deep space exploration [6]. However, the low energy conversion efficiency of current TE materials restricts the widespread application of TE technology. The performance of TE materials is evaluated using a dimensionless thermoelectric figure-of-merit called the ZT value ($ZT = S^2\sigma T/\kappa$), where S, σ, T, and κ represent the Seebeck coefficient, the electrical conductivity, the absolute temperature, and the thermal conductivity respectively [7]. Given the strong coupling between S, σ, and κ [8–10], obtaining TE materials with a high ZT is a huge challenge.

GeTe is a widely applied p-type TE material with high intrinsic ZT value and optimization prospects in the mid-temperature range. Previous studies have shown that GeTe has a high intrinsic carrier concentration ($n = \sim10^{21}$ cm^{-3}), resulting in a low intrinsic S (~30 μV K^{-1}), and a high intrinsic κ (~8 W m^{-1} K^{-1}) [11,12]. These parameters indicate a large gap must be bridged to reach the level of practical application. Additionally, GeTe exhibits a rhombohedral phase structure (R–GeTe) at room temperature and undergoes a phase transition from rhombohedral to cubic phase (C–GeTe), which exhibits better TE properties than R-GeTe, at approximately 700 K. In addition, this phase transition process is detrimental to the stability of materials [13,14]. Therefore, many studies have attempted to achieve the TE properties optimization of GeTe with success by suppressing the phase transition, increasing the S, and reducing the κ. For instance, Zheng et al. explored the use of Mn-Sb co-doped GeTe and demonstrated that by promoting multi-energy band convergence and introducing microstructures like dislocations, they were able to enhance the material's ZT value by approximately 47% [15]. Similarly, Ming et al. achieved successful

optimization by utilizing Li-Sb co-doped GeTe [16], effectively suppressing the phase transition at room temperature. By manipulating the charge distribution, they facilitated multi-energy band convergence and enhanced phonon scattering, resulting in the remarkable enhancement of the material's *ZT* value by approximately 51%. In addition, there are currently various methods such as introduction of resonance levels, band convergence and hyperconvergence to improve the thermoelectric performance of GeTe [17–20].

Nonetheless, although there are certain processes which would help in the case of low solubility limits of the dopants [21], the development of TE materials with new superior properties through elemental doping currently faces the challenge brought about by the solid solubility limit of elements [15,22,23]. In recent research on high-entropy RE cobaltates (LaNdPrSmEu)$_{1-x}$Sr$_x$CoO$_3$ (x = 0, 0.05, 0.1) and Lu-Sb/Bi co-doped GeTe [24,25], the co-doping of REs with other elements enables larger solubility in the materials than single doping. This phenomenon is caused by the large radius and electronegativity differences according to the Hume–Rothery rule and Darken–Gurry maps [25,26]. Furthermore, REs possess more valence electrons than Ge and local magnetic moments and simultaneously reduce the *n* and increase the *S*, finally enhancing the power factor (*PF* = *S*^{2}*σ*) [27,28]. Moreover, REs, which have larger atomic mass (*M*) and atomic radius (*R*) than Ge, are more effective in developing multiscale microstructures, enhancing phonon alloying scattering, and reducing the κ_L [29]. Considering that adding REs in small amounts (less than 1 mol.%) significantly improves the TE properties, REs co-doping is a cost-effective strategy in TE materials modification.

In this study, a Mn-Sb co-doped GeTe-based TE sample, Ge$_{0.86}$Mn$_{0.1}$Sb$_{0.04}$Te, was prepared using the melt-quenching method combined with Fast Hot Pressing (FHP) sintering. The doping concentrations of Mn and Sb were selected based on previous studies [15]. The addition of Mn promotes the convergence of multiple energy bands, and Sb regulates the carrier concentration to be closer to the optimal value and compensates for the carrier mobility reduction, in deep enable satisfied electrical transport properties. Additionally, we incorporated 1 mol.% of REs into the GeMnSbTe matrix, resulting in Ge$_{0.86}$Mn$_{0.1}$Sb$_{0.04}$Te + 1 mol.% RE (RE =Er, Tm, Yb, Lu). The selection of rare earth dopants is based on the factors of same main group as Sb and Te, large atomic radius and electronegativity difference, and the presence or absence of local magnetic moment. The addition of REs increases the solid solubility of Mn in GeTe. Moreover, the cubic phase structure at room temperature, enhancement of *PF*, and reduction of *κ* are simultaneously achieved. Notably, we achieved an improvement in the peak figure-of-merit (*ZT*$_{max}$) and average figure-of-merit (*ZT*$_{ave}$) of Ge$_{0.86}$Mn$_{0.1}$Sb$_{0.04}$Te + 1 mol.% Tm within the temperature range of 450–800 K, with respective increases of 72.98% and 69.66% compared to Ge$_{0.86}$Mn$_{0.1}$Sb$_{0.04}$Te. Overall, this study demonstrates the effectiveness of optimizing the TE performance of REs-doped GeMnSbTe TE materials and analyzes the main reasons behind this optimization.

2. Experimental Methods

2.1. Experimental preparation

The thermoelectric material samples of Ge$_{0.86}$Mn$_{0.1}$Sb$_{0.04}$Te + 1 mol. % RE (RE = Er, Tm, Yb, Lu) were prepared using the melt-quenching method combined with FHP sintering. High-purity monolithic Ge particles (99.999%), Mn blocks (99.999%), Sb particles (99.999%), Te particles (99.999%), and REs, including Eu, Tm, Yb, and Lu particles (99.999%), were weighed and dosed according to the stoichiometric ratio. These particles were then vacuum sealed in a quartz glass tube with a vacuum degree lower than 2×10^{-3} Pa. The glass tube was placed in a muffle furnace and slowly heated to 1050 ℃, maintaining the temperature for 24 h. After the heat preservation, the glass tube was removed and quenched in cold water. The samples were then annealed in a tube furnace at 500 ℃ for 100 min, followed by a 72 h hold before

cooling to room temperature. The ingot was taken out, crushed, and ground into powder for FHP and sintering at a pressure of 50 MPa and a temperature of 500 ℃. Block samples with densities above 99% were produced. The blocks were wire-cut into specific sizes for subsequent testing and characterization.

2.2. Performance testing and structure characterization

The phase composition of the samples was determined through X–ray diffraction (XRD) tests (PANalytical, the Netherlands) and Differential Scanning Calorimeter (DSC) tests (Netzsch STA 449 F5). The lattice constants and angles were obtained by conducting structural refinement. The microstructure of the samples was characterized using Scanning electron microscopy (SEM, Scios 2, Czech) and double spherical aberration corrected transmission electron microscopy (TEM, Spectra 300). To assess the electrical transport properties, measurements were taken using a Seebeck coefficient test system (CTA–3) at room temperature up to 773 K. The carrier concentration n_H and carrier mobility μ_H were determined using a Hall effect tester (PMS–9) at 300 K and a magnetic field of $\pm$ 1 T. The thermal diffusion coefficient λ of the sample was measured using a laser thermal conductivity meter (LFA500), while the density ρ was obtained through Archimedes' drainage method. The specific heat value C_p of the sample was calculated using the Dulong–Petit law. Finally, the total thermal conductivity κ of the sample was determined by multiplying λ, C_p, and ρ. By utilizing the measured Seebeck coefficient *S* and conductivity σ, the electronic thermal conductivity κ_e of the sample was calculated using the Wiedemann–Franz relationship, which further allowed the determination of the lattice thermal conductivity κ_L of the sample.

2.3. Density functional theory (DFT) Calculations

DFT calculations were employed using the projector augmented wave (PAW) method in the Vienna Ab-initio Simulation Package (VASP), and the exchange−correlation energy was calculated within the generalized gradient approximation (GGA) using the Perdew−Burke−Ernzerhof (PBE) functional. The electronic wave functions were expanded using a plane wave basis set with an energy cutoff of 500 eV. All structures were relaxed until the residual forces on the free atoms were smaller than 0.005 eV/Å. Geometry optimizations were carried out using Monkhorst-Pack type k-point meshes of 3 × 3 × 3. The electronic structure analysis was assistant by vaspkit. Meanwhile, Atomic Simulation Environment (ASE) and VESTA software were used for model building. We constructed a 2 × 2 × 2 supercell for the cubic structures Ge$_{32}$Te$_{32}$ and Ge$_{31}$TmTe$_{32}$.

3. Results and discussion

3.1. Phase structure and composition analysis

The XRD patterns of the samples before and after FHP at room temperature are shown in Fig. 1a and b. Prior to FHP, Ge impurity peaks could be observed, which basically disappeared after FHP. This phenomenon indicates that the FHP process reduces elemental segregation and enhances the crystallinity of the materials. Fig. 1c provides a closer look at the (200) and (220) peaks of the samples after FHP. When the (220) peak appears as a double peak, the sample corresponds to R–GeTe, while a single peak corresponds to the C–GeTe. At room temperature, doping with Er, Tm, and Lu transforms R to C–GeTe, which exhibits a higher lattice symmetry and is beneficial to band convergence and *S* enhancement [30]. However, the samples doped with Yb do not undergo phase transition. Fig. 1d shows the variation of lattice constants *a*, *c*, and *γ* with the angle values obtained by structural refinement of the samples [31]. The above results are also illustrated in the DSC results in Fig. 2. The phase transition of the sample Ge$_{0.86}$Mn$_{0.1}$Sb$_{0.04}$Te without REs occurs at 658 K in Fig. 2a. No phase transition peaks appear in the DSC

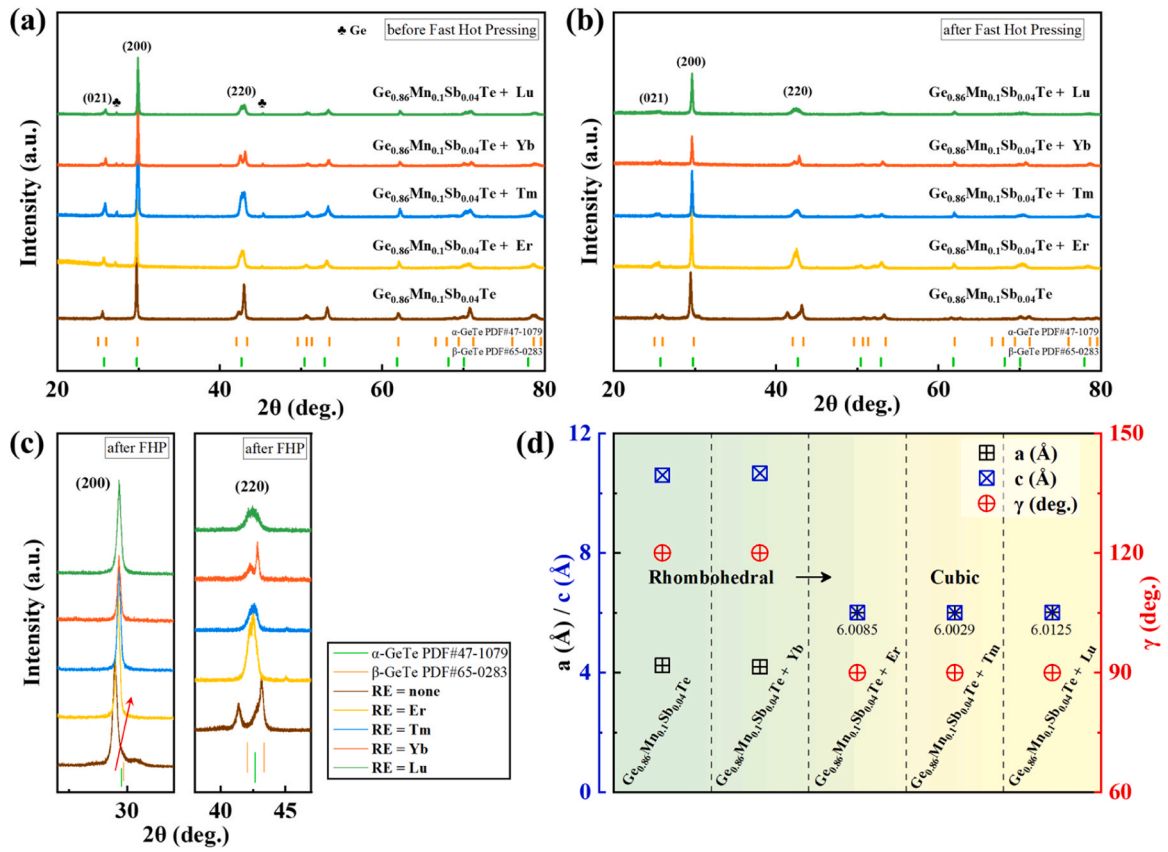**Fig. 1.** XRD patterns of $Ge_{0.86}Mn_{0.1}Sb_{0.04}Te$ + 1 mol.% RE (RE = none, Er, Tm, Yb, Lu) (a) before and (b) after FHP, (c) zoomed-in the (220) and (200) peaks of samples after FHP, and (d) lattice constants and angles obtained by structural refinement of the samples.
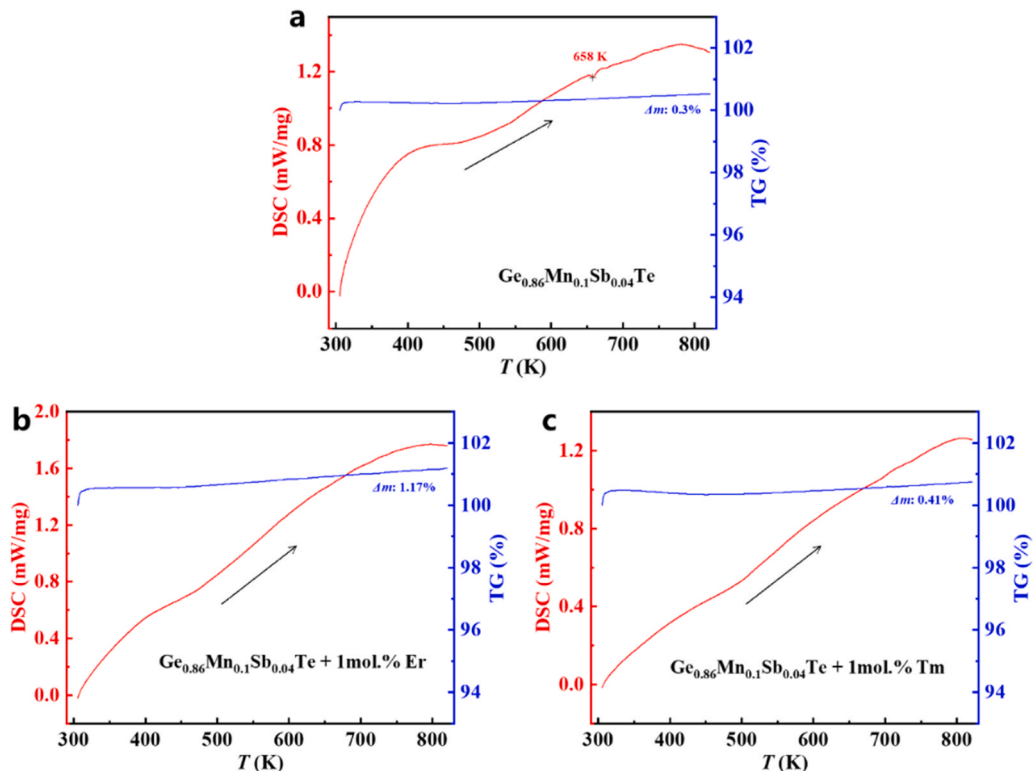

Fig. 2. DSC curves of $Ge_{0.86}Mn_{0.1}Sb_{0.04}Te$ + 1 mol.% RE: (a) RE = none, (b) RE = Er, (c) RE = Tm.

curves of the Er-doped and Tm-doped samples (Fig. 2b and c), which indicates that the phase transition temperature of the samples is reduced to below room temperature, and the samples maintain the cubic phase structure. Having a cubic phase structure with high symmetry is advantageous for the improvement of the Seebeck coefficient [32], which is confirmed in the performance test section. Compare to $Ge_{0.86}Mn_{0.1}Sb_{0.04}Te$ without REs, the (200) peak shifts to a high angle after doping with REs, which is due to the fact that the electronegativity difference between REs and Te is larger than that between Ge and Te, shortens the average bond length and causes the lattice shrinkage [33]. At the same time, due to the sequential increase in the substitution limit, the (200) peak of the Tm, Er, Lu, and Yb-doped samples gradually shifts to a lower angle due to lattice expansion.

In addition, adding REs increases the solid solubility of Mn in this material system. As shown in Fig. 3, the energy-dispersive spectroscopy (EDS) mapping results reveal that the actual Mn content of the samples without RE doping is 2.95 atom.%, it increases to approximately 5 atom. % after the doping of REs. Furthermore, Fig. 3a demonstrates that unsolved Mn elements exists in the form of some nanoscale to micrometer precipitates in sample $Ge_{0.86}Mn_{0.1}Sb_{0.04}Te$ while Sb and Te elements are uniformly distributed. Fig. 3a–e illustrates that the doping amounts of REs in the samples are all within 1 atom.%. The samples doped with REs have a small amount of Ge precipitation, which is consistent with the XRD patterns. However, existing research shows that the small amount of Ge precipitation has a negligible effect on the TE properties of the prepared GeTe-based samples [29,34,35].

3.2. Electrical transport characteristics

Fig. 4a–c illustrate the electrical transport characteristics of the $Ge_{0.86}Mn_{0.1}Sb_{0.04}Te + 1$ mol.% RE (RE = none, Er, Tm, Yb, Lu). As depicted in Fig. 4a, all the samples exhibit a positive Seebeck coefficient, indicating their p-type TE material classification. Upon doping the $Ge_{0.86}Mn_{0.1}Sb_{0.04}Te$ sample with 1 mol.% of REs, a significant increase in S is observed, particularly in the medium and high-temperature range. Notably, $Ge_{0.86}Mn_{0.1}Sb_{0.04}Te + 1$ mol.% Yb demonstrates the highest S of 172.82 $\mu V K^{-1}$. The substitution of REs at the Ge site can act as an electron donation, reducing the n_H, thereby increasing the S [22]. Some of the REs possessing local magnetic moment can also lead to the enhancement of S [28]. The local magnetic moment can induce the spin

Seebeck effect, which can be simply understood as the "spin electric potential" generated by the temperature gradient, thereby increasing the Seebeck coefficient. Moreover, the enhancement in the solid solubility of Mn caused by REs plays a crucial role in increasing S. Mn doping with GeTe facilitates the convergence of multiple energy bands within the material [15,36], thereby positively influencing its electrical transport properties. Zheng et al. conducted a study on the energy band structure of cubic $Ge_{27-x}Mn_xTe_{27}$ (x = 0, 1, 2) using DFT calculations. They observed that as the number of Mn atoms increased, the energy difference between the light and heavy valence bands decreased from 0.21 eV to 0.05 eV and then to 0.01 eV, indicating its role in promoting energy band convergence [15]. Zhi et al. also used DFT to calculate the energy band structure of C–$Ge_{27}Te_{27}$ and C–$Ge_{24}Mn_3Te_{27}$ and found that the band gap (E_g) increased from 0.17 eV to 0.33 eV [1]. They also observed the convergence of multivalence bands.

In addition, the doping of Sb and Tm elements in GeTe can also adjust the electronic band structure of the material to a certain extent. Suresh et al. obtained the result that doping Sb in GeTe can promote the band convergence in their work [37]. As for the REs, we conducted the DFT calculations of cubic $Ge_{32}Te_{32}$ and $Ge_{31}TmTe_{32}$ to analyze their effects on the band structure. As shown in Fig. 5a and b, the E_g increases to 0.44 eV from 0.38 eV after the Tm atom added. VB_1 to VB_5 are the first to the fifth valence band maximum of the structures. Noticeably, the energy offsets of ΔE_{1-4} ($|E_{VB1} - E_{VB4}| = 0.188$ eV) and ΔE_{1-5} ($|E_{VB1} - E_{VB5}| = 0.262$ eV) in C-$Ge_{32}Te_{32}$ are higher than that in C-$Ge_{31}TmTe_{32}$ ($\Delta E_{1-4} = 0.133$ eV and $\Delta E_{1-5} = 0.173$ eV), which indicates that the dopant Tm can promote the convergence of the VB_4 and VB_5 bands in GeTe.

As shown in Fig. 5c, the density-of-state effective mass m^* of the sample $Ge_{0.86}Mn_{0.1}Sb_{0.04}Te$ presented in the Pisarenko curve calculated with the single parabolic band (SPB) model is 2.44 m_0, where m_0 is the electron mass. The m^* of the sample increases after the REs is added, the m^* fitting value of the four REs doped samples is 2.81 m_0. That means at the same carrier concentration, the samples doped with REs exhibit a higher Seebeck coefficient than sample $Ge_{0.86}Mn_{0.1}Sb_{0.04}Te$. Therefore, the high lattice symmetry of the cubic phase and the convergence of multiple energy bands increase the band degeneracy N_V, resulting in the enhancement of m^* and S. To prove the promoting effect of increasing the Mn content on electrical transport properties, a sample with a higher Mn-Sb co-doping content, $Ge_{0.72}Mn_{0.2}Sb_{0.08}Te$, was prepared in this study. Its Seebeck coefficient is considerably higher (170.36 $\mu V/K$) than

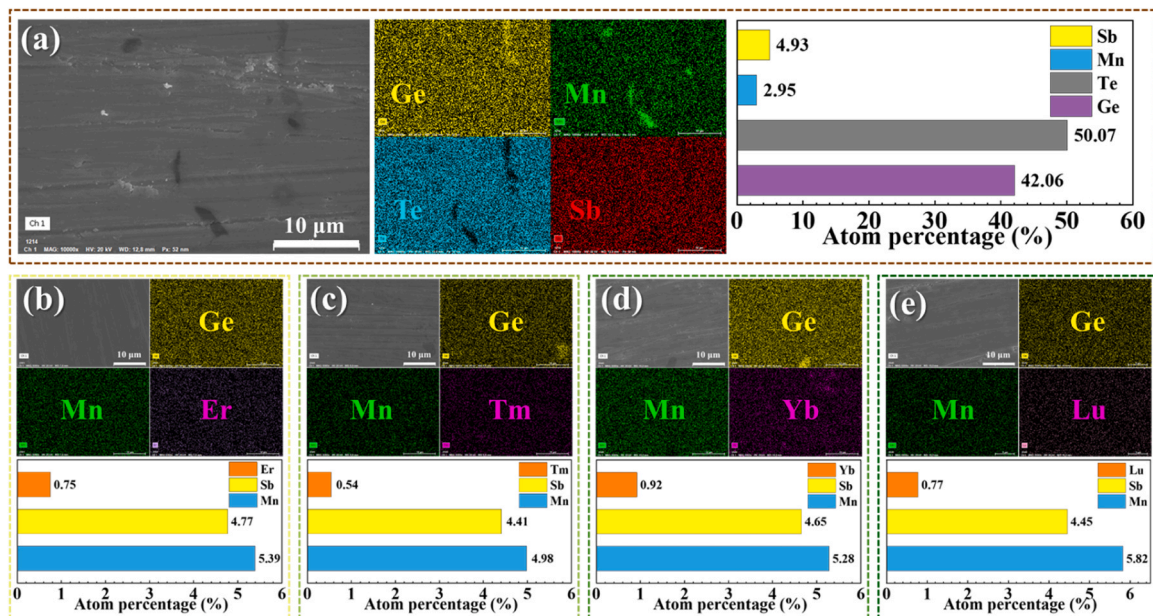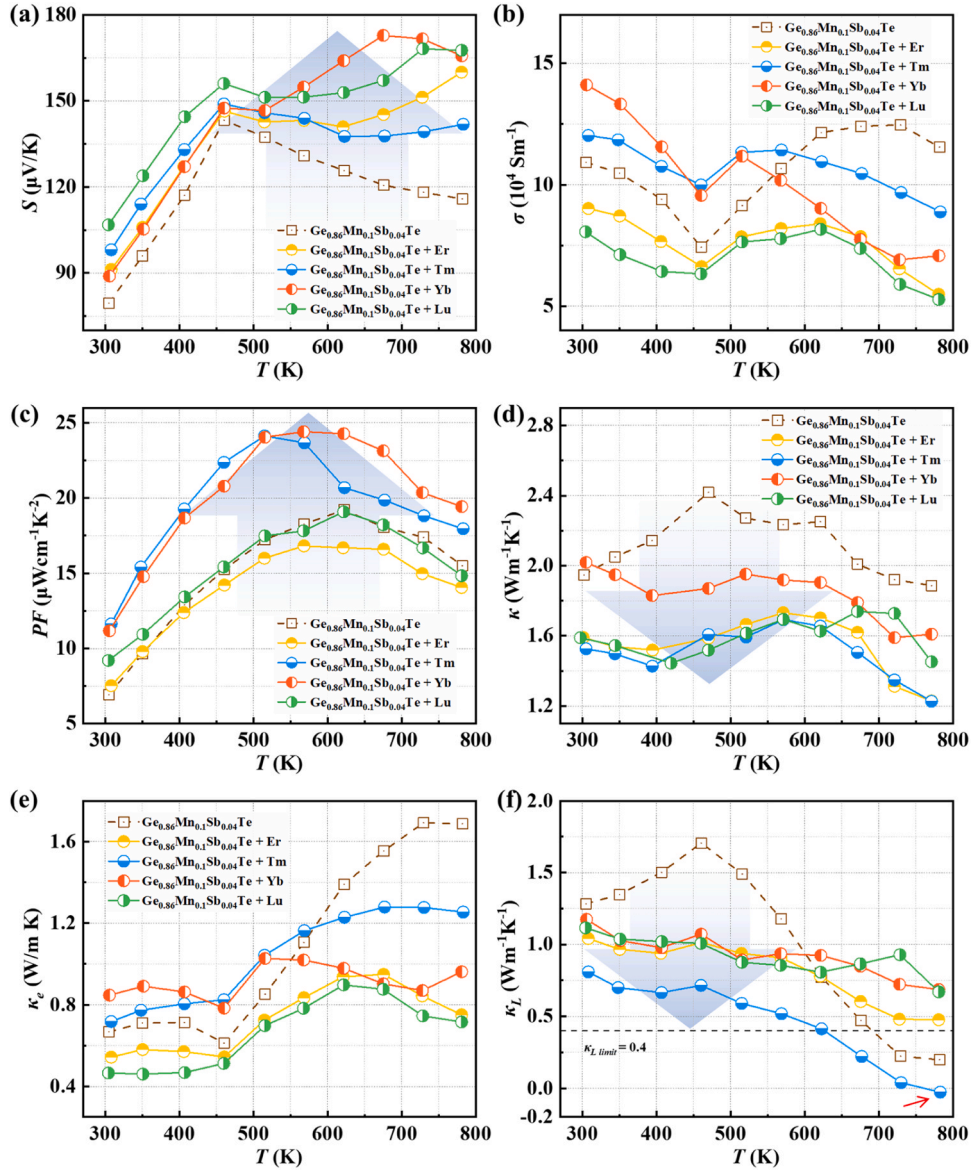**Fig. 3.** SEM images, EDS mapping images and analysis of $Ge_{0.86}Mn_{0.1}Sb_{0.04}Te + 1$ mol.% RE: (a) RE = none, (b) RE = Er, (c) RE = Tm, (d) RE = Yb, (e) RE = Lu.

Fig. 4. (a) Seebeck coefficient, (b) conductivity, (c) power factor, (d) total thermal conductivity, (e) electronic thermal conductivity, (f) lattice thermal conductivity of $Ge_{0.86}Mn_{0.1}Sb_{0.04}Te$ + 1 mol.% RE (RE = none, Er, Tm, Yb, Lu) versus temperature.
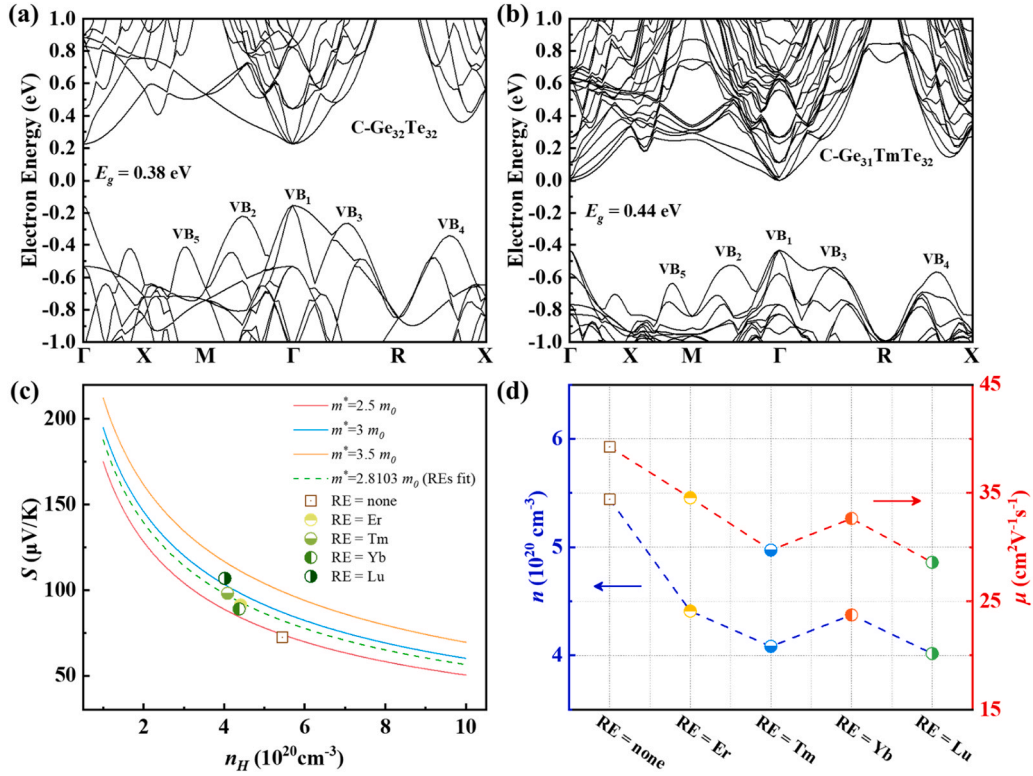
that of $Ge_{0.86}Mn_{0.1}Sb_{0.04}Te$.

However, the band flattening upon Mn and the alloy scattering by multi elements doping lead to a significant decrease in carrier mobility μ_H and a subsequent decrease in conductivity σ [1], as depicted in Fig. 4b. To address this issue, heterovalent Sb (+3) substitution in Ge (+2) sites can be implemented to optimize the n_H and bring it nearer the optimal carrier concentration (5×10^{19} cm^{-3}) of GeTe [38]. Moreover, REs, which have many valence electrons, can further reduce the n_H [22]. This compensation helps improve the electrical transport properties despite the loss in μ_H. The results of the Hall effect test in Fig. 5d confirms this process, showing a decrease in carrier concentration from 5.44×10^{20} cm^{-3} for $Ge_{0.86}Mn_{0.1}Sb_{0.04}Te$ to $< 4.5 \times 10^{20}$ cm^{-3} for REs doped samples. Additionally, at approximately 460 K, the sample exhibits a bipolar effect (downturn in the plot of S versus T) that negatively affects its TE performance at high temperatures [39–41]. Nevertheless, this bipolar effect can be somewhat mitigated by increasing the content of Mn/Sb or adding REs. Finally, the maximum PF of Yb-doped and Tm-doped samples increased from 19.21 μW cm^{-1} K^{-2} ($Ge_{0.86}Mn_{0.1}Sb_{0.04}Te$, 623 K) to 24.41 μW cm^{-1} K^{-2} (573 K) and 24.13 μW cm^{-1} K^{-2} (523 K). The PF of the other samples did not change

significantly as shown in Fig. 4c. Although these changes in electrical transport properties have a relatively small impact on the final ZT value, the ZT value can be improved further by simultaneously optimizing the thermal transport properties.

3.3. Thermal transport characteristics

The thermal transport characteristics of $Ge_{0.86}Mn_{0.1}Sb_{0.04}Te$ + 1 mol.% RE (RE = none, Er, Tm, Yb, Lu), including its total thermal conductivity κ, electronic thermal conductivity κ_e, and lattice thermal conductivity κ_L, are plotted in Fig. 4d–f, respectively. After incorporating REs into $Ge_{0.86}Mn_{0.1}Sb_{0.04}Te$, the κ of the sample decreased to varying degrees across the entire temperature range. The addition of 1% molar percentage of Er, Tm, Yb, and Lu reduced the lowest κ value of the samples from the original 1.89 W m^{-1} K^{-1} (773 K) to 1.23 W m^{-1} K^{-1} (773 K), 1.23 W m^{-1} K^{-1} (773 K), 1.59 W m^{-1} K^{-1} (723 K), and 1.44 W m^{-1} K^{-1} (423 K), respectively, as shown in Fig. 4d. The κ_e is determined using the Wiedemann–Franz law [42], as described by Eq. (1):

Fig. 5. Electronic band structure of (a) $Ge_{32}Te_{32}$ and (b) $Ge_{31}TmTe_{32}$, (c) Room-temperature S as a function of n_H, (d) comparison of n_H and μ_H for $Ge_{0.86}Mn_{0.1}Sb_{0.04}Te$ + 1 mol.% RE (RE = none, Er, Tm, Yb, Lu).

$$\kappa_e = L\sigma T. \tag{1}$$

The Lorentz number (L) used in Eq. (1) can be calculated using Eq. (2) [43]:

$$L = 1.5 + \exp\frac{-|S|}{116}, \tag{2}$$

Finally, the κ_L of the sample can be obtained using Eq. (3):

$$\kappa_L = \kappa - \kappa_e. \tag{3}$$

As shown in Fig. 4f, the κ_L of $Ge_{0.86}Mn_{0.1}Sb_{0.04}Te$ + 1 mol.% RE (RE = none, Er, Tm, Yb, Lu) decreases significantly compared with that of $Ge_{0.86}Mn_{0.1}Sb_{0.04}Te$ in the medium and low-temperature range.

However, at high temperatures, the κ_L of the $Ge_{0.86}Mn_{0.1}Sb_{0.04}Te$ + 1 mol.% Tm reaches a physically impossible negative value at 773 K, which means the Wiedemann–Franz law indicating strong phonon-electron coupling does not hold for this sample at high temperatures (> 673 K). Despite this, the results of this work still indicate that the incorporation of REs in sample $Ge_{0.86}Mn_{0.1}Sb_{0.04}Te$ significantly reduces the κ_L to below 1 W m^{-1} K^{-1} in the medium and low-temperature range, approaching the amorphous limit value of 0.4 W m^{-1} K^{-1} for GeTe [31].

For the κ_e that has coupling properties with the electrical transport properties, the κ_L of the sample is relatively independent of the electrical transport properties [44]. To investigate the reasons for the decrease in
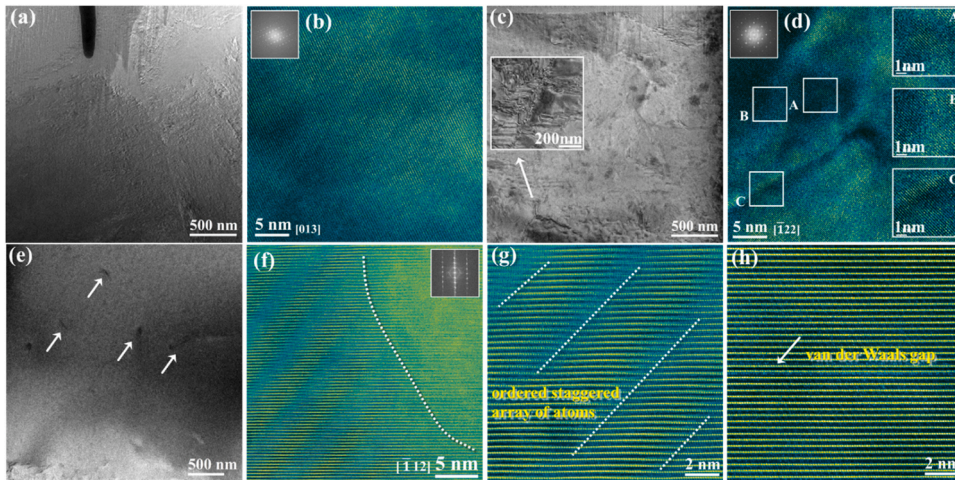
Fig. 6. TEM images of some samples. (a) and (b) are the low- and high-resolution images of $Ge_{0.86}Mn_{0.1}Sb_{0.04}Te$, (c) and (d) are the low- and high-resolution images of sample $Ge_{0.86}Mn_{0.1}Sb_{0.04}Te$ + 1 mol.% Er, (e) is the low-resolution image of $Ge_{0.72}Mn_{0.2}Sb_{0.08}Te$, and (f–h) are the atomic phase images of $Ge_{0.72}Mn_{0.2}Sb_{0.08}Te$. The insets therein are all local magnification and FFT plots. (The colors of the high-resolution and atomic phase images have been modified).

κ_L, the microstructure of some samples was analyzed using double-spherical aberration TEM. Fig. 6**a and b** display the low- and high-resolution TEM images of $Ge_{0.86}Mn_{0.1}Sb_{0.04}Te$. The TEM image appears smooth and uniform, revealing clear grain boundaries. The corresponding high-resolution (HRTEM) image exhibits good uniformity and some strain contrast but no obvious microscopic defect structure. Fig. 6**c and d** present the low- and high-resolution TEM images of $Ge_{0.86}Mn_{0.1}Sb_{0.04}Te + 1$ mol.% Er. The TEM image illustrates the nano-domain structure introduced by 1 mol.% Er [45], while the HRTEM image reveals a significant inhomogeneity and layer dislocation structure within the sample. This phenomenon suggests that lattice distortion is widely present throughout the sample. Hence, different atomic arrangements can be found in different regions (A, B, and C) of Fig. 6**d**, with these arrangements being interconnected by a considerable number of dislocations across the entire region. Fig. 6**e** shows the TEM morphology of $Ge_{0.72}Mn_{0.2}Sb_{0.08}Te$, while Fig. 6**f–h** depict the scanning transmission electron microscopy (STEM) atomic phase diagrams corresponding to it. The TEM image reveals areas of microstructural enrichment resulting from changes in the ratio of incorporated elements. In this sample, an ordered staggered array of atoms is observed on the left side of the white dotted line in Fig. 6**f**, as shown in the enlarged view in Fig. 6**g**. Additionally, Fig. 6**h** illustrates the introduction of a van der Waals gap consisting of Ge vacancies [46–48]. The figures confirm that rich microstructures are introduced into the samples under the combined effect of the doping of REs and their promotion of Mn solid solubility. These different microstructures, which are achieved through Mn-Sb co-doping and RE doping with GeTe, effectively enhance the alloying scattering of phonons in the material, resulting in a significant reduction in κ_L at all temperatures.

$Ge_{0.86}Mn_{0.1}Sb_{0.04}Te + 1$ mol.% Tm exhibits the lowest κ_L at all temperatures. The TEM images of this sample reveal a highly diverse microstructure, as shown in Fig. 7. The TEM image in Fig. 7**a** captures the micromorphology of dislocation enrichment, dislocation networks, and nano precipitation phases. Fig. 7**b–d** provides separate morphology images of these three structures. Further analysis through EDS mapping scanning and magnification observation was conducted on the nano precipitation phase, as depicted in Fig. 7**e**. The analysis reveals that this phase is enriched with Sb and Te, exhibiting sizes ranging from a few nanometers to tens of nanometers. Notably, each nanophase displays a cavity at its edge. The presence of these dispersed and abundant nano precipitation phases adds complexity and richness to the microstructure of the sample, thereby enhancing phonon scattering. Fig. 7**f** presents the HRTEM image of this sample, revealing prominent inhomogeneities that suggest random atom replacement and stress distribution due to lattice distortion. The inset showcases the FFT (Fast Fourier Transform) image, which displays amorphous rings, indicating the amorphization of the sample. Additionally, magnified images of regions A and B of Fig. 7**f** are provided in the right inset, indicating the presence of interstitial and

vacancy clusters throughout the region, which are caused by radius differences between elements [49,50]. Overall, the microstructure exhibits a diverse range of features, including dislocation enrichment, dislocation networks, nano precipitation phases with vacancy structures, interstitial clusters, and vacancy clusters.

These features, combined with the effects of distortion and amorphization, contribute to the enhancing of phonon scattering. Specifically, phonons with different frequencies are subjected to effective scattering processes caused by lattice anharmonicity. These processes include the Umklapp and Normal mechanisms, which are particularly powerful. Furthermore, high-frequency phonons experience scattering due to differences in mass and strain caused by point defects. In addition, mid-frequency phonons encounter scattering effects originating from dislocation cores and the strain fields associated with dislocations. In contrast, low-frequency phonons are scattered by interfaces within nanostructures. Finally, a significant reduction in κ_L through phonon scattering enhancement is reached [51].

3.4. Optimization of the figure-of-merit ZT

By combining the electrical and thermal transport properties of the samples, the TE figure-of-merit *ZT* values are obtained and shown in Fig. 8**a**. When the REs are doped in $Ge_{0.86}Mn_{0.1}Sb_{0.04}Te$, the *ZT* values show varying degrees of enhancement from room temperature to 773 K, particularly in the high-temperature section. Fig. 8**b** compares the average *ZT* values of the series of samples in the temperature range of 450–800 K (the application temperature range of GeTe–based TE materials) and the peak *ZT* values obtained in the temperature range from room temperature to 773 K. $Ge_{0.86}Mn_{0.1}Sb_{0.04}Te + 1$ mol.% Tm exhibits a ZT_{max} of 1.15 at 773 K and a ZT_{ave} (450–800 K) of 0.87, representing a 72.98% and 69.66% enhancement over the $Ge_{0.86}Mn_{0.1}Sb_{0.04}Te$, respectively. The substitution of Mn-Sb/REs at the Ge site leads to a decrease in the μ_H of the samples, but it also results in a significant increase in the *S* of the samples to compensate for the decrease in μ_H. Additionally, the κ of the samples decreases significantly with the substitution of these elements, ultimately resulting in increased *ZT* values.

Table 1 summarizes the results of element-doped GeTe-based TE materials and related optimization reports in the literatures [15,16,25, 27,48,52–55]. The ZT_{max} enhancement percentage represents the percentage of ZT_{max} enhancement achieved by the sample with the peak *ZT* value mentioned in the literature compared with the intrinsic samples (GeTe in the literatures). The findings reveal that the performance enhancement in this study exhibit a significant advantage over the existing related work, which demonstrates the effectiveness of TE performance optimization by incorporating REs to Mn-Sb co-doped GeTe.
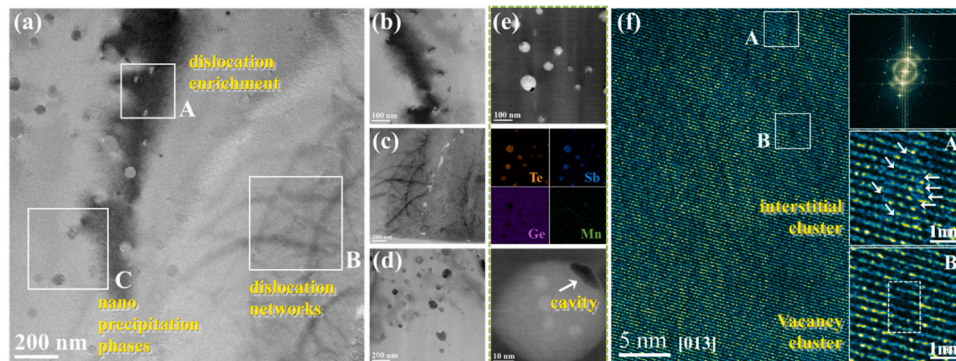
Fig. 7. TEM images of $Ge_{0.86}Mn_{0.1}Sb_{0.04}Te + 1$ mol.% Tm. (a)–(d) are low-resolution TEM images, (e) are low- and high-resolution images and EDS mapping scanning result plots, and (f) is a high-resolution image with insets showing localized magnification and FFT plots. (The colors of the high-resolution images have been modified).
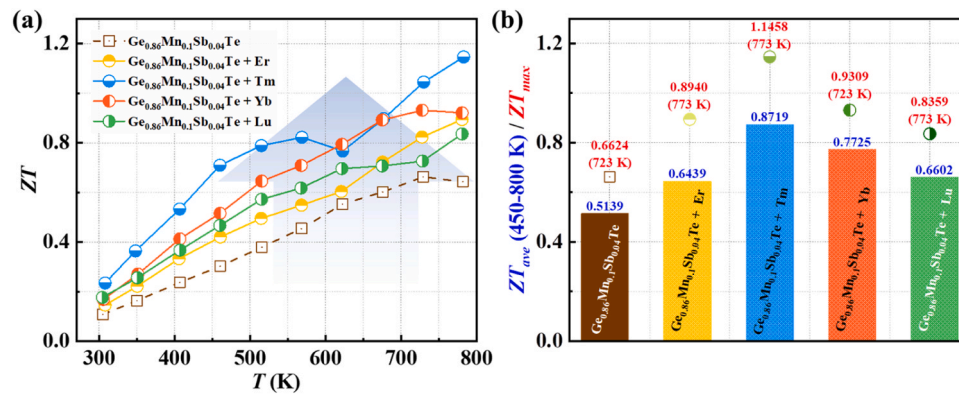
Fig. 8. (a) ZT values of $Ge_{0.86}Mn_{0.1}Sb_{0.04}Te + 1$ mol.% RE versus temperature, (b) Comparison of ZT_{ave} (450–800 K) and ZT_{max} (room temperature to 773 K).

Table 1
Element-doped GeTe-based TE materials and related optimization results reported in the literatures.

Doping element	ZT_{max} enhancement percentage [%]	ZT_{max} value	Microstructure observed	Reference
Er/Tm/Yb/Lu (to $Ge_{0.86}Mn_{0.1}Sb_{0.04}Te$)	73	1.15 (773 K)	ordered atomic staggered arrays, van der Waals interstitials, dislocation enrichment, dislocation networks, nano precipitation phases with cavity structures, interstitial clusters, and vacancy clusters	This work
Pb (to GeTe)	~58.82	0.81 (673 K)	/	[52]
Sb (to GeTe)	~8.19	~1.90 (760 K)	The fine Ge precipitates, twins and nano-domains	[53]
Bi (to GeTe)	~45.45	2.0 (773 K)	Dispersive nano-precipitates, Ge vacancies in the form of van der Waals gaps	[48]
Mn (to GeTe)	Do not enhance	/	/	[15]
Mn-Sb (to GeTe)	47.0	1.61 (823 K)	Dislocations, stacking faults and lattice loss	[15]
Zr (to GeTe)	~73.39	1.9 (673 K)	Widespread defect–related structures, stacking faults or dislocations	[54]
Li-Sb (to GeTe)	~50.79	1.90 (723 K)	R→C phase transfer	[16]
Li-Bi (to GeTe)	~35.71	~1.5 (623 K)	Ge second phase	[55]
Eu/Gd/Er/Tm (to GeTe)	~18.75	~1.3 (723 K)	Ge second phase	[27]
Lu (to GeTe)	~27.96	1.5 (673 K)	Condensed point defects	[25]
Sb-Lu (to GeTe)	~49.29	1.75 (673 K)	/	[25]

4. Conclusion

Compare to $Ge_{0.86}Mn_{0.1}Sb_{0.04}Te$ without REs doping, this study achieves 26–73% enhancements in the peak ZT value and 25–70% enhancements in the average ZT value in the temperature range of 450–800 K in $Ge_{0.86}Mn_{0.1}Sb_{0.04}Te + 1$ mol.% RE (RE =Er, Tm, Yb, Lu). The ZT_{max} of $Ge_{0.86}Mn_{0.1}Sb_{0.04}Te + 1$ mol.% Tm reaches 1.15, and the ZT_{ave} (450–800 K) reaches 0.87. The reasons for the successful performance improvement are summarized in three aspects: the successful promotions of the transformation of samples from the rhombic phase to the cubic phase at room temperature (phase transition engineering). This transformation is achieved by co-doping with different ratios of Mn-Sb elements and adding REs on the basis of the Mn-Sb co-doping. Additionally, this study enhances the Seebeck coefficient to compensate for the reduced electrical mobility and conductivity. This enhancement is achieved by promoting the convergence of energy bands and decreasing the carrier concentration, resulting in an enhancement of the power factor of the samples (energy band engineering). Furthermore, the study introduces micro-defects of different scales to enhance phonon scattering and strongly reduce the lattice thermal conductivity of the materials (phonon engineering). All of these processes demonstrate the effectiveness of the optimization methods in this study.

CRediT authorship contribution statement

Huang Wenjing: Writing – review & editing, Writing – original draft, Visualization, Validation, Software, Project administration, Methodology, Investigation, Formal analysis, Data curation, Conceptualization. **Chen Feida:** Writing – review & editing, Visualization, Supervision, Resources, Project administration, Funding acquisition, Data curation, Conceptualization. **Wu Shujie:** Writing – review & editing, Validation, Methodology, Formal analysis. **Tang Xiaobin:** Writing – review & editing, Visualization, Supervision, Resources, Project administration, Funding acquisition, Conceptualization.

Declaration of Competing Interest

The authors declare that they have no known competing financial interests or personal relationships that could have appeared to influence the work reported in this paper.

Data Availability

Data will be made available on request.

Acknowledgements

References

[1] S. Zhi, J. Li, L. Hu, J. Li, N. Li, H. Wu, F. Liu, C. Zhang, W. Ao, H. Xie, X. Zhao, S. J. Pennycook, T. Zhu, Medium entropy-enabled high performance cubic GeTe thermoelectrics, Adv. Sci. 8 (2021) 2100220, https://doi.org/10.1002/advs.202100220.

[2] Y. Jin, D. Ren, Y. Qiu, L. Zhao, Electrical and thermal transport properties of $Ge_{1-x}Pb_xCu_ySb_yTeSe_{2y}$, Adv. Funct. Mater. (2023) 2304512, https://doi.org/10.1002/adfm.202304512.

[3] L.E. Bell, Cooling, heating, generating power, and recovering waste heat with thermoelectric systems, Science 321 (2008) 1457–1461, https://doi.org/10.1126/science.1158899.

[4] J. He, T.M. Tritt, Advances in thermoelectric materials research: Looking back and moving forward, Science 357 (2017) eaak9997, https://doi.org/10.1126/science.aak9997.

[5] B. Jiang, W. Wang, S. Liu, Y. Wang, C. Wang, Y. Chen, L. Xie, M. Huang, J. He, High figure-of-merit and power generation in high-entropy GeTe-based thermoelectrics, Science 377 (2022) 208–213, https://doi.org/10.1126/science.abq5815.

[6] Z. Guo, G. Wu, X. Tan, R. Wang, Z. Zhang, G. Wu, Q. Zhang, J. Wu, G. Liu, J. Jiang, Enhanced Thermoelectric Performance in GeTe by Synergy of Midgap state and Band Convergence, Adv. Funct. Mater. 33 (2023) 2212421, https://doi.org/10.1002/adfm.202212421.

[7] Ioffe, A.F., L.S. Stil'bans, E.K. Iordanishvili, T.S. Stavitskaya, A. Gelbtuch and George H. Vineyard. "Semiconductor Thermoelements and Thermoelectric Cooling." (1957). ⟨https://doi.org/10.1063/1.3060810⟩.

[8] D. Zhang, B. Zhang, Z. Zhou, G. Wang, Z. Cheng, P. Jiang, H. Wu, P. Chen, G. Han, G. Wang, X. Zhou, X. Lu, High Thermoelectric Performance in Cu_2SnS_3 by Control Over Phase-Dependent Mobility Edge, Adv. Energy Mater. 13 (2023) 2301406, https://doi.org/10.1002/aenm.202301406.

[9] J. Karni, The thermoelectric alternative, Nat. Mater. 10 (2011) 481–482, https://doi.org/10.1038/nmat3057.

[10] A.J. Minnich, M.S. Dresselhaus, Z.F. Ren, G. Chen, Bulk nanostructured thermoelectric materials: current research and future prospects, Energy Environ. Sci. 2 (2009) 466, https://doi.org/10.1039/b822664b.

[11] W. Liu, D. Wang, Q. Liu, W. Zhou, Z. Shao, Z. Chen, High-performance GeTe-based thermoelectrics: from materials to devices, Adv. Energy Mater. 10 (2020) 2000367, https://doi.org/10.1002/aenm.202000367.

[12] X. Zhang, Z. Bu, S. Lin, Z. Chen, W. Li, Y. Pei, GeTe thermoelectrics, Joule 4 (2020) 986–1003, https://doi.org/10.1016/j.joule.2020.03.004.

[13] T. Chatterji, C.M.N. Kumar, U.D. Wdowik, Anomalous temperature-induced volume contraction in GeTe, Phys. Rev. B. 91 (2015) 054110, https://doi.org/10.1103/PhysRevB.91.054110.

[14] Y. Jin, D. Wang, Y. Qiu, L.-D. Zhao, Boosting the thermoelectric performance of GeTe by manipulating the phase transition temperature via Sb doping, J. Mater. Chem. C 9 (2021) 6484–6490, https://doi.org/10.1039/D1TC01714D.

[15] Z. Zheng, X. Su, R. Deng, C. Stoumpos, H. Xie, W. Liu, Y. Yan, S. Hao, C. Uher, C. Wolverton, M.G. Kanatzidis, X. Tang, Rhombohedral to Cubic Conversion of GeTe via MnTe Alloying Leads to Ultralow Thermal Conductivity, Electronic Band Convergence, and High Thermoelectric Performance, J. Am. Chem. Soc. 140 (2018) 2673–2686, https://doi.org/10.1021/jacs.7b13611.

[16] M. Liu, J. Zhu, B. Cui, F. Guo, Z. Liu, Y. Zhu, M. Guo, Y. Sun, Q. Zhang, Y. Zhang, W. Cai, J. Sui, High-performance lead-free cubic GeTe-based thermoelectric alloy, Cell Rep. Phys. Sci. 3 (2022) 100902, https://doi.org/10.1016/j.xcrp.2022.100902.

[17] D.K. Bhat, U.S. Shenoy, Mg/Ca doping ameliorates the thermoelectric properties of GeTe: Influence of electronic structure engineering, J. Alloy. Compd. 843 (2020) 155989, https://doi.org/10.1016/j.jallcom.2020.155989.

[18] U.S. Shenoy, G.K. D, D.K. Bhat, Probing of Bi doped GeTe thermoelectrics leads to revelation of resonant states, J. Alloy. Compd. 921 (2022) 165965, https://doi.org/10.1016/j.jallcom.2022.165965.

[19] D.K. Bhat, U.S. Shenoy, Resonance levels in GeTe thermoelectrics: zinc as a new multifaceted dopant, N. J. Chem. 44 (2020) 17664–17670, https://doi.org/10.1039/D0NJ04273K.

[20] H. Kim, S.K. Kihoi, U.S. Shenoy, J.N. Kahiu, D.H. Shin, D.K. Bhat, H.S. Lee, High thermoelectric and mechanical performance achieved by a hyperconverged electronic structure and low lattice thermal conductivity in GeTe through $CuInTe_2$ alloying, J. Mater. Chem. A 11 (2023) 8119–8130, https://doi.org/10.1039/D2TA09280H.

[21] S. Shenoy, D.K. Bhat, Enhanced bulk thermoelectric performance of $Pb_{0.6}Sn_{0.4}Te$: effect of magnesium doping, J. Phys. Chem. C. 121 (2017) 20696–20703, https://doi.org/10.1021/acs.jpcc.7b07017.

[22] S. Perumal, S. Roychowdhury, D.S. Negi, R. Datta, K. Biswas, High thermoelectric performance and enhanced mechanical stability of *p*-type $Ge_{1-x}Sb_xTe$, Chem. Mater. 27 (2015) 7171–7178, https://doi.org/10.1021/acs.chemmater.5b03434.

[23] J. Li, X. Zhang, X. Wang, Z. Bu, L. Zheng, B. Zhou, F. Xiong, Y. Chen, Y. Pei, High-Performance GeTe Thermoelectrics in Both Rhombohedral and Cubic Phases, J. Am. Chem. Soc. 140 (2018) 16190–16197, https://doi.org/10.1021/jacs.8b09147.

[24] A. Kumar, D. Dragoe, D. Berardan, N. Dragoe, Thermoelectric properties of high-entropy rare-earth cobaltates, J. Mater. 9 (2023) 191–196, https://doi.org/10.1016/j.jmat.2022.08.001.

[25] W.-Y. Lyu, W.-D. Liu, M. Li, X.-L. Shi, M. Hong, T. Cao, K. Guo, J. Luo, J. Zou, Z.-G. Chen, Condensed point defects enhance thermoelectric performance of rare-earth Lu-doped GeTe, J. Mater. Sci. Technol. 151 (2023) 227–233, https://doi.org/10.1016/j.jmst.2023.01.004.

[26] Y. Mae, What the darken–gurry plot means about the solubility of elements in metals, Met. Mater. Trans. A 47 (2016) 6498–6506, https://doi.org/10.1007/s11661-016-3730-1.

[27] S. Acharya, D. Dey, T. Maitra, A. Soni, A. Taraphder, Rare earth doping and effective band-convergence in SnTe for improved thermoelectric performance, Appl. Phys. Lett. 113 (2018) 193904, https://doi.org/10.1063/1.5055250.

[28] E.M. Levin, S.L. Bud'ko, K. Schmidt-Rohr, Enhancement of thermopower of TAGS-85 high-performance thermoelectric material by doping with the rare earth dy, Adv. Funct. Mater. 22 (2012) 2766–2774, https://doi.org/10.1002/adfm.201103049.

[29] W.-Y. Lyu, W.-D. Liu, M. Li, M. Hong, K. Guo, J. Luo, J. Xing, Q. Sun, S. Xu, J. Zou, Z.-G. Chen, The effect of rare earth element doping on thermoelectric properties of GeTe, Chem. Eng. J. 446 (2022) 137278, https://doi.org/10.1016/j.cej.2022.137278.

[30] B. Jiang, Y. Yu, H. Chen, J. Cui, X. Liu, L. Xie, J. He, Entropy engineering promotes thermoelectric performance in p-type chalcogenides, Nat. Commun. 12 (2021) 3234, https://doi.org/10.1038/s41467-021-23569-z.

[31] P. Li, T. Ding, J. Li, C. Zhang, Y. Dou, Y. Li, L. Hu, F. Liu, C. Zhang, Positive effect of Ge vacancies on facilitating band convergence and suppressing bipolar transport in GeTe-based alloys for high thermoelectric performance, Adv. Funct. Mater. 30 (2020) 1910059, https://doi.org/10.1002/adfm.201910059.

[32] S.A.J. Kimber, J. Zhang, C.H. Liang, G.G. Guzmán-Verri, P.B. Littlewood, Y. Cheng, D.L. Abernathy, J.M. Hudspeth, Z.-Z. Luo, M.G. Kanatzidis, T. Chatterji, A. J. Ramirez-Cuesta, S.J.L. Billinge, Dynamic crystallography reveals spontaneous anisotropy in cubic GeTe, Nat. Mater. 22 (2023) 311–315, https://doi.org/10.1038/s41563-023-01483-7.

[33] O. Ivanov, M. Yaprintsev, R. Lyubushkin, O. Soklakova, Enhancement of thermoelectric efficiency in Bi2Te3 via rare earth element doping, Scr. Mater. 146 (2018) 91–94, https://doi.org/10.1016/j.scriptamat.2017.11.031.

[34] L. Yue, T. Fang, S. Zheng, W. Cui, Y. Wu, S. Chang, L. Wang, P. Bai, H. Zhao, Cu/Sb codoping for tuning carrier concentration and thermoelectric performance of GeTe-based alloys with ultralow lattice thermal conductivity, ACS Appl. Energy Mater. 2 (2019) 2596–2603, https://doi.org/10.1021/acsaem.8b02213.

[35] M. Li, M. Hong, X. Tang, Q. Sun, W.-Y. Lyu, S.-D. Xu, L.-Z. Kou, M. Dargusch, J. Zou, Z.-G. Chen, Crystal symmetry induced structure and bonding manipulation boosting thermoelectric performance of GeTe, Nano Energy 73 (2020) 104740, https://doi.org/10.1016/j.nanoen.2020.104740.

[36] Z. Liu, J. Sun, J. Mao, H. Zhu, W. Ren, J. Zhou, Z. Wang, D.J. Singh, J. Sui, C.-W. Chu, Z. Ren, Phase-transition temperature suppression to achieve cubic GeTe and high thermoelectric performance by Bi and Mn codoping, Proc. Natl. Acad. Sci. USA 115 (2018) 5332–5337, https://doi.org/10.1073/pnas.1802020115.

[37] S. Perumal, P. Bellare, U.S. Shenoy, U.V. Waghmare, K. Biswas, Low thermal conductivity and high thermoelectric performance in Sb and Bi codoped GeTe: complementary effect of band convergence and nanostructuring, Chem. Mater. 29 (2017) 10426–10435, https://doi.org/10.1021/acs.chemmater.7b04023.

[38] Z. Bu, W. Li, J. Li, X. Zhang, J. Mao, Y. Chen, Y. Pei, Dilute Cu2Te-alloying enables extraordinary performance of r-GeTe thermoelectrics, Mater. Today Phys. 9 (2019) 100096, https://doi.org/10.1016/j.mtphys.2019.100096.

[39] L. Hu, F. Meng, Y. Zhou, J. Li, A. Benton, J. Li, F. Liu, C. Zhang, H. Xie, J. He, Leveraging deep levels in narrow bandgap $Bi_{0.5}Sb_{1.5}Te_3$ for record-High zT_{ave} near room temperature, Adv. Funct. Mater. 30 (2020) 2005202, https://doi.org/10.1002/adfm.202005202.

[40] R. Liu, H. Chen, K. Zhao, Y. Qin, B. Jiang, T. Zhang, G. Sha, X. Shi, C. Uher, W. Zhang, L. Chen, Entropy as a gene-like performance indicator promoting thermoelectric materials, Adv. Mater. 29 (2017) 1702712, https://doi.org/10.1002/adma.201702712.

[41] Z. Deng, A. Olvera, J. Casamento, J.S. Lopez, L. Williams, R. Lu, G. Shi, P.F. P. Poudeu, E. Kioupakis, Semiconducting high-entropy chalcogenide alloys with ambi-ionic entropy stabilization and ambipolar doping, Chem. Mater. 32 (2020) 6070–6077, https://doi.org/10.1021/acs.chemmater.0c01555.

[42] N. Stojanovic, D.H.S. Maithripala, J.M. Berg, M. Holtz, Thermal conductivity in metallic nanostructures at high temperature: Electrons, phonons, and the Wiedemann-Franz law, Phys. Rev. B. 82 (2010) 075418, https://doi.org/10.1103/PhysRevB.82.075418.

[43] H.-S. Kim, Z.M. Gibbs, Y. Tang, H. Wang, G.J. Snyder, Characterization of Lorenz number with Seebeck coefficient measurement, APL Mater. 3 (4) (2015) 041506, https://doi.org/10.1063/1.4908244.

[44] A. Shakouri, Recent developments in semiconductor thermoelectric physics and materials, Annu. Rev. Mater. Res. 41 (2011) 399–431, https://doi.org/10.1146/annurev-matsci-062910-100445.

[45] Y. Jiang, J. Dong, H.-L. Zhuang, J. Yu, B. Su, H. Li, J. Pei, F.-H. Sun, M. Zhou, H. Hu, J.-W. Li, Z. Han, B.-P. Zhang, T. Mori, J.-F. Li, Evolution of defect structures leading to high ZT in GeTe-based thermoelectric materials, Nat. Commun. 13 (2022) 6087, https://doi.org/10.1038/s41467-022-33774-z.

[46] P. Chen, H. Wu, B. Zhang, Z. Zhou, S. Zheng, L. Dai, Y. Huo, D. Zhang, Y. Yan, K. Peng, G. Han, X. Lu, X. Zhou, G. Wang, Intrinsically low lattice thermal conductivity and anisotropic thermoelectric performance in In-doped $GeSb_2Te_4$

single crystals, Adv. Funct. Mater. 33 (2023) 2211281, https://doi.org/10.1002/adfm.202211281.

[47] Y. Yu, L. Xie, S.J. Pennycook, M. Bosman, J. He, Strain-induced van der Waals gaps in GeTe revealed by in situ nanobeam diffraction, Sci. Adv. 8 (2022) eadd7690, https://doi.org/10.1126/sciadv.add7690.

[48] D. Wu, D. Feng, X. Xu, M. He, J. Xu, J. He, Realizing high figure of merit plateau in Ge Bi Te via enhanced Bi solution and Ge precipitation, J. Alloy. Compd. 805 (2019) 831–839, https://doi.org/10.1016/j.jallcom.2019.07.120.

[49] Y. Xiao, H. Wu, J. Cui, D. Wang, L. Fu, Y. Zhang, Y. Chen, J. He, S.J. Pennycook, L.-D. Zhao, Realizing high performance n-type PbTe by synergistically optimizing effective mass and carrier mobility and suppressing bipolar thermal conductivity, Energy Environ. Sci. 11 (2018) 2486–2495, https://doi.org/10.1039/C8EE01151F.

[50] Y. Xiao, H. Wu, W. Li, M. Yin, Y. Pei, Y. Zhang, L. Fu, Y. Chen, S.J. Pennycook, L. Huang, J. He, L.-D. Zhao, Remarkable roles of Cu To synergistically optimize phonon and carrier transport in n-Type PbTe-Cu $_2$ Te, J. Am. Chem. Soc. 139 (2017) 18732–18738, https://doi.org/10.1021/jacs.7b11662.

[51] Z. Chen, Z. Jian, W. Li, Y. Chang, B. Ge, R. Hanus, J. Yang, Y. Chen, M. Huang, G. J. Snyder, Y. Pei, Lattice dislocations enhancing thermoelectric PbTe in addition to band convergence, Adv. Mater. 29 (2017), https://doi.org/10.1002/adma.201606768.

[52] S.P. Li, J.Q. Li, Q.B. Wang, L. Wang, F.S. Liu, W.Q. Ao, Synthesis and thermoelectric properties of the (GeTe)1-x(PbTe)x alloys, Solid State Sci. 13 (2011) 399–403, https://doi.org/10.1016/j.solidstatesciences.2010.11.045.

[53] H. Tan, B. Zhang, G. Wang, Y. Chen, X. Shen, L. Guo, X. Han, X. Lu, X. Zhou, Rapid preparation of Ge0.9Sb0.1Te1+ via unique melt spinning: Hierarchical microstructure and improved thermoelectric performance, J. Alloy. Compd. 774 (2019) 129–136, https://doi.org/10.1016/j.jallcom.2018.09.144.

[54] X. Bai, C. Liu, F. Li, Z. Zhang, Y. Peng, R. Si, B. Feng, G. Wu, J. Gao, H. Wei, L. Miao, Tailoring 5s2 lone pair-antibonding orbital interaction by Zr-doping to realize ultrahigh power factor in thermoelectric GeTe, Chem. Eng. J. 461 (2023) 142069, https://doi.org/10.1016/j.cej.2023.142069.

[55] F. Guo, M. Liu, J. Zhu, Z. Liu, Y. Zhu, M. Guo, X. Dong, Q. Zhang, Y. Zhang, W. Cai, J. Sui, Suppressing lone-pair expression endows room-temperature cubic structure and high thermoelectric performance in GeTe-based materials, Mater. Today Phys. 27 (2022) 100780, https://doi.org/10.1016/j.mtphys.2022.100780.